X-ray Spectroscopic Characterization of Co(IV) and Metal−Metal Interactions in Co$_4$O$_4$: Electronic Structure Contributions to the Formation of High-Valent States Relevant to the Oxygen Evolution Reaction

Ryan G. Hadt,[†] Dugan Hayes,[†] Casey N. Brodsky,[∥] Andrew M. Ullman,[∥] Diego M. Casa,[‡] Mary H. Upton,[‡] Daniel G. Nocera,*[,∥] and Lin X. Chen*[,†,§]

[†]Chemical Sciences and Engineering Division and [‡]Advanced Photon Source, Argonne National Laboratory, Lemont, Illinois 60439, United States

[§]Department of Chemistry, Northwestern University, Evanston, Illinois 60208, United States

[∥]Department of Chemistry and Chemical Biology, Harvard University, Cambridge, Massachusetts 02138, United States

Ⓢ Supporting Information

ABSTRACT: The formation of high-valent states is a key factor in making highly active transition-metal-based catalysts of the oxygen evolution reaction (OER). These high oxidation states will be strongly influenced by the local geometric and electronic structures of the metal ion, which are difficult to study due to spectroscopically active and complex backgrounds, short lifetimes, and limited concentrations. Here, we use a wide range of complementary X-ray spectroscopies coupled to DFT calculations to study Co(III)$_4$O$_4$ cubanes and their first oxidized derivatives, which provide insight into the high-valent Co(IV) centers responsible for the activity of molecular and heterogeneous OER catalysts. The combination of X-ray absorption and 1s3p resonant inelastic X-ray scattering (Kβ RIXS) allows Co(IV) to be isolated and studied against a spectroscopically active Co(III) background. Co K- and L-edge X-ray absorption data allow for a detailed characterization of the 3d-manifold of effectively localized Co(IV) centers and provide a direct handle on the t$_{2g}$-based redox-active molecular orbital. Kβ RIXS is also shown to provide a powerful probe of Co(IV), and specific spectral features are sensitive to the degree of oxo-mediated metal−metal coupling across Co$_4$O$_4$. Guided by the data, calculations show that electron−hole delocalization can actually oppose Co(IV) formation. Computational extension of Co$_4$O$_4$ to CoM$_3$O$_4$ structures (M = redox-inactive metal) defines electronic structure contributions to Co(IV) formation. Redox activity is shown to be linearly related to covalency, and M(III) oxo inductive effects on Co(IV) oxo bonding can tune the covalency of high-valent sites over a large range and thereby tune E^0 over hundreds of millivolts. Additionally, redox-inactive metal substitution can also switch the ground state and modify metal−metal and antibonding interactions across the cluster.
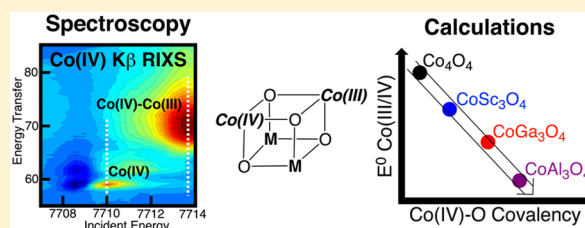
INTRODUCTION

The generation and storage of solar fuels is highly dependent on the efficiency of the oxygen evolution reaction (OER).[1−4] With the discovery of the proclivity of metalate oxidic clusters to promote OER,[5−8] research in the area has turned toward making better oxygen evolution catalysts (OECs) through geometric and electronic structural perturbations, which may involve metal substitution or alloying.[9−14] To understand the origin(s) of increased activity and to define structure/function relationships, the geometric and electronic structural perturbations of catalytic centers in their resting and active states need to be defined. Yet, reaction intermediates in OEC catalytic processes are often minority species in largely spectroscopically active backgrounds, thus severely limiting their detection and characterization. X-ray absorption spectroscopy (XAS) can be powerful in uncovering potential intermediates, as band edges can be sensitive to metal oxidation state. While metal K-edge

XAS measurements in the hard X-ray regime can be insightful for both geometric and electronic structures, soft X-ray experiments provide access to metal L- and M-edges, which are subject to different selection rules and are more sensitive to electronic structure due to stronger interactions between 2p/3p and 3d electrons.[15] To this end, resonant inelastic X-ray scattering (RIXS) has become a powerful spectroscopic probe that provides "soft X-ray-like" data using hard X-rays,[16−18] opening the way for probing specific inner-shell processes with higher energy resolution and selectivity for various sample environments. In addition, as a two-photon process, RIXS provides rich and spectroscopically distinct information content relative to the single-photon X-ray absorption.[15−18]

Properties intrinsic to heterogeneous catalysts such as geometric strain,[19−22] molecular encagement,[23−25] and redox-leveling[26] often allow for greater activity in the conversion of unreactive substrates. In defining the structure/function relationships that are at the root of this greater activity, comparisons drawn between molecular and heterogeneous analogs are beneficial.[27] Nonetheless, the design of homogeneous inorganic complexes as models of heterogeneous OEC catalysts is difficult to achieve, and few bona fide examples exist where both structure and activity are replicated. In recent years, inorganic molecular clusters have been developed as potential water oxidation catalysts, inspired by the Mn_4CaO_5 cluster of photosystem II (PSII) OEC.[28−30] An intensively studied heterogeneous/homogeneous pair with regard to OEC is the cobalt phosphate $(CoP_i)/Co_4O_4$ cubane pair, respectively, as CoP_i comprises Co_4O_4 cubanes as its basic structural element.[31,32] Co_4O_4 structures with different ligand sets (Figure 1 shows the $Co_4O_4(OAc)_4(py)_4$ primary ligation sphere) have
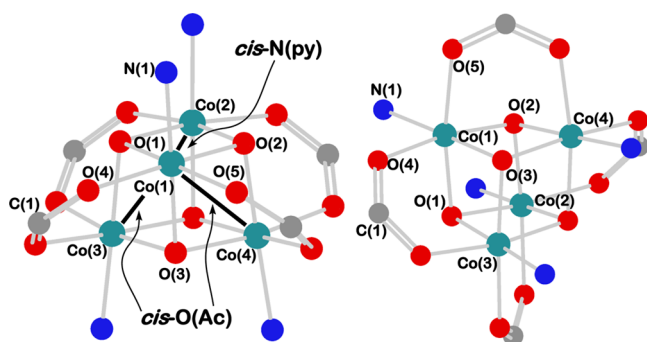

Figure 1. Different perspectives of the core structure of $Co_4O_4(OAc)_4(py)_4$ with (left) N(py) axial and (right) O(Ac) axial. Acetate and pyridine ligands have been truncated for clarity.

been synthesized and characterized[33−40] and they have been intensively researched as molecular mimics of CoP_i.[41−53] The active sites of CoP_i are Co(IV) centers, and indeed, Co_4O_4 cubanes can house $S = ^1/_2$ Co(IV) centers that exhibit electron paramagnetic resonance (EPR) signals comparable to those observed for Co(IV) in activated catalyst films.[51,52] The multifrequency EPR results (at <10 K) indicate that the Co(IV) spin density is symmetrically delocalized over the Co_4O_4 core,[52] and the X-ray crystal structure of the oxidized cubane has also been interpreted as fully delocalized.[53] These observations are related to the degree of electron−hole delocalization over the Co_4O_4 core, which can be described in terms of mixed-valency [i.e., effectively $Co(3.25)_4$ vs $Co(IV)Co(III)_3$]. In the Robin and Day classification, the effective oxidation states of the metals in a mixed-valent (MV) complex can be described as class I, II, or III.[54] The classification is dependent on the relative magnitudes of the vibronic trapping force vs the electronic coupling matrix element, H_{AB}. Class I complexes contain localized metal oxidation states at all temperatures, using all spectroscopic methodologies (i.e., strong vibronic trapping force, typically provided by asymmetric ligand fields, and small H_{AB}). At the other extreme, class III complexes give rise to spectral features reflecting average, effective oxidation states at all temperatures, using most spectroscopic methods (large H_{AB}, strong delocalization). In the latter case, it should be noted, even in the case of class III complexes, that core-hole spectroscopies can provide spectral features reflecting individual oxidation

states.[55] The class II regime has a low-energy barrier for intramolecular ET (i.e., small vibronic trapping force, moderate H_{AB}, and delocalization) and typically exhibits either localized or delocalized characteristics, depending on spectroscopic time scale and/or temperature. Thus, the aforementioned results suggest significant class III mixed-valent (MV) character for oxidized Co_4O_4 on the EPR time scale (~$10^{−9}$ s).[54]

The ability to form high-valent Co(IV) within the Co_4O_4 topology has been attributed to efficient electron−hole delocalization,[41,47,56] which is also coupled to the formation of reactive species.[41,47,50] In CoP_i, the minimalist active core is composed of two adjacent formal Co(IV) centers, which promote the proton-coupled electron transfer (PCET) reactivity needed for water splitting.[31,57] Additionally, Co(IV) in CoP_i thin films likely facilitates PCET-driven conduction between active sites and the electrode via Co(III)/(IV) self-exchange or hopping,[31,50,58−60] which can be related directly to class II/III MV character.[54,61−65] Akin to the results for CoP_i, two electron−holes [formally 2Co(III)/2Co(IV)] have been proposed to be necessary for the observed OER activity of the $Co_4O_4(OAc)_4(py)_4$ cubane.[41,47] In light of the importance of Co(IV) in both CoP_i and cubane systems, direct spectroscopic detection and characterization of high-valent, partially or fully delocalized MV species is crucial to developing comparative structure activity relations between molecular and heterogeneous OEC catalysts.

Herein we utilize a combination of Co K- and L-edge X-ray absorption spectroscopies as well as 1s3p ($K\beta$) RIXS as sensitive probes of the geometric and electronic structures of Co_4O_4 cubanes. The combined XAS/RIXS measurements provide a powerful means of "mapping" Co(IV) contributions in these systems against a spectroscopically complex background. The XAS/RIXS methods effectively probe "localized" Co(IV) electronic structure, in part due to the intrinsically faster time scale of the inner-shell electronic transitions in X-ray spectroscopic measurements (~$10^{−15}$ s) relative to EPR (~$10^{−9}$ s). Both Co K-edge and L-edge XAS provide direct characterization of the low-spin 3d-manifold of Co(IV). Specific spectral features present in the Co K-edge and 1s3p RIXS have uncovered oxo-mediated metal−metal (M/M) interactions that are crucial to the basic electronic structure of the cubane core. The experimental data, combined with electronic structure calculations, indicate that the redox active molecular orbital (RAMO) of Co_4O_4 is relatively ionic, which can result from electron−hole delocalization and oppose Co(IV) formation. These observations have been extended to cubanes with substituted redox inactive metals (e.g., CoM_3O_4, M = Al, Ga, or Sc) to provide further insight into the interplay between electron−hole delocalization and the formation of high-valent species in a Co(IV) oxidic framework. These results together provide new insights into the redox transport and activity of molecular and heterogeneous OEC catalysts composed of cubane cores.

■ RESULTS

Co K-Edge XANES. The Co K-edge XANES spectra for the neutral Co(III)$_4$ (**1**) and oxidized Co(IV)Co(III)$_3$ (**2**) states of the $Co_4O_4(OAc)_4(py)_4$ cubane are given in Figure 2. The pre-edge region (labeled 1s → 3d in Figure 2) is given in the inset; pre-edge and edge energies of **1** are ~7709.6 and 7722.1 eV, respectively. Upon one-electron oxidation, the edge energy of **2** shifts by ca. +0.4 eV to ~7722.5 eV and the pre-edge shift is very slight (<0.2 eV). These XAS shifts upon oxidation are
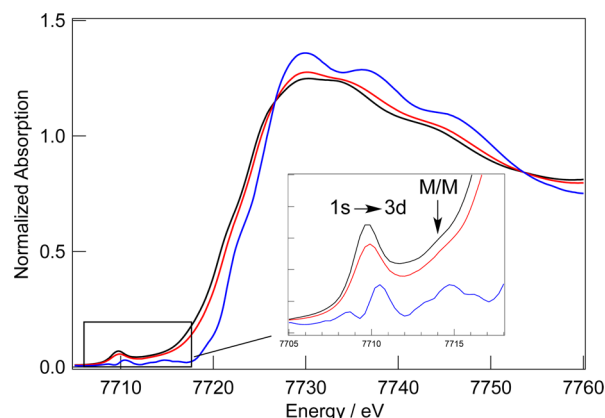
Figure 2. Co K-edge XAS: **1** (black line), **2** (red line), and Co(IV) (blue line). Co(IV) spectrum has been renormalized to the edge jump. Inset: expanded region of the pre-edge.

consistent with a partial increase in Z_{eff}. Another feature is observed at ~7714 eV (labeled M/M in Figure 2, vide infra) for both **1** and **2**, and its intensity does not appear to vary significantly with oxidation.

The rates of intramolecular self-exchange ET for delocalized class III complexes are on the order of ~10^{12} s^{-1}.[64,65] Given the ultrafast nature of the core-hole lifetimes (~1−4 fs), XAS provides an opportunity to spectroscopically resolve delocalized MV electronic structure. The formation of a core-hole potential in the final state will also result in partial or full localization.[55] Thus, the data are treated in terms of localized Co(IV) and Co(III) sites, and an approximate "Co(IV)" spectrum can be obtained by taking a scaled difference spectrum of **1** from **2** [i.e., $\mathbf{2} - (^3/_4)\mathbf{1}$]. It is noted that the subtraction method does not account for potential differences in Co(III)−ligand covalency and bond distances between **1** and **2**; however, for simplicity and the purposes of the work described herein, will use a metal oxidation state formalism and describe the oxidation as Co(IV) with the caveat that the oxidation may have some parentage involving oxygen. That said, the subtracted spectra exhibit strong similarities to iso-electronic, low-spin d^5 systems. The renormalized Co(IV) spectrum (Figure 2, blue spectrum) has an edge energy of ~7723.4 eV (~1.3 eV higher in energy relative to **1**), consistent with a complete Co oxidation state change from Co(III) to Co-(IV).[7,66] The pre-edge region of Co(IV) exhibits a split structure, similar to isoelectronic, low-spin d^5 Fe(III) complexes[67] and Fe(III) in Fe(II)/Fe(III) mixed-valence complexes;[68] pre-edge peak maxima are at ~7708.6 and 7710.5 eV (Δ = 1.9 eV). For low-spin octahedral Fe(III) complexes, these peaks have been assigned as 1s → 3d transitions and correlate to the $(t_{2g})^6$ and $(t_{2g})^5(e_g)^1$ excited final states. Co(IV) also exhibits another broad feature centered at ~7714.5 eV, which is similar in energy to **1** but more pronounced. Similar features have been observed in α-Fe$_2$O$_3$[69] and LiCoO$_2$.[70,71]

Co K-edge EXAFS. The Co K-edge k^3-weighted EXAFS spectra and their Fourier transforms are given in Figure 3. The R-space data of **1** (black line, Figure 3A) shows intense features at R values of ~2.8 and 1.9 Å (at R ~ 2.35 and 1.4 Å, respectively, in Fourier transformed spectra without phase correction) associated with Co−Co and Co−O/N vectors, respectively. The spectrum of **2** shows a broadening and decreased amplitude of the Co−Co feature, consistent with
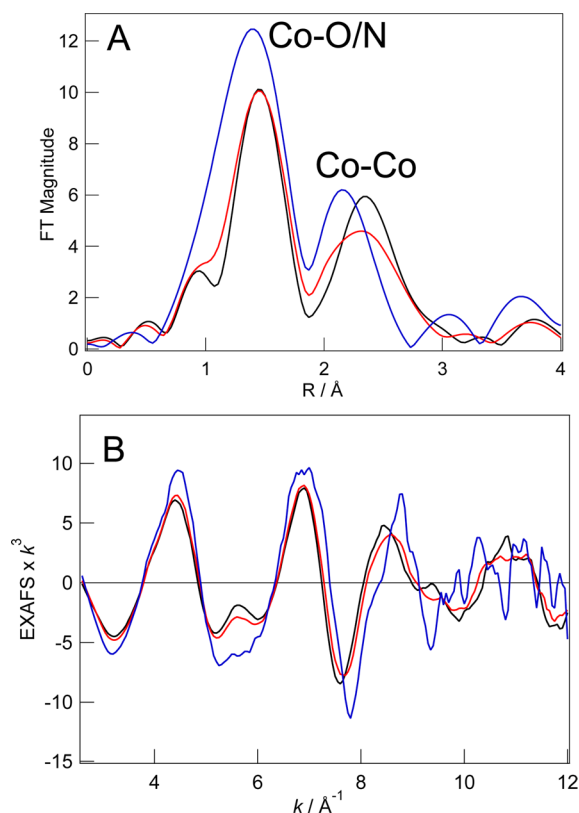

Figure 3. Co K-edge EXAFS data: (A) Fourier transforms and (B) k^3-weighted EXAFS oscillations of **1** (black line), **2** (red line), and Co(IV) (blue line).

multiple oxidation states arising from a mixture of Co(IV) and Co(III) in the oxidized Co$_4$O$_4$ cluster. The EXAFS data have been obtained from the weighted difference spectrum of Co(IV) from above [blue line in Figure 2, $\mathbf{2} - (^3/_4)\mathbf{1}$]. The Co−Co feature of Co(IV) is now similar in spectral width and intensity to that of Co(III) in **1**. The Co−Co and Co−O/N features of Co(IV) shift to slightly shorter R-values due to increased Z_{eff}.

Due to the presence of multiple different O/N and Co−Co distances, a full fit to the EXAFS data would be under-determined. However, the experimental EXAFS data of **1** and Co(IV) can still be well-modeled using the neutral and Co(IV) DFT distorted geometries, respectively. These results are given in Table S1 and Figure S1 of the Supporting Information (SI). For more details, see the text below Table S1 (SI). The first-shell for **1** (Co−O/N in Figure 3) can be modeled with three shorter Co−O (~1.87 Å) and three longer Co−O/N bonds (~1.94 Å). The Co−Co peak can be modeled with two Co−Co single-scattering pathways of ~2.73 and 2.85 Å and one other single-scattering pathway [Co−C(1), 2.86 Å, N (degeneracy) = 2]. The longer Co−Co vector arises from the Co(1)−Co(2) interaction [N = 1; see Figure 1, cis-N(py)]. The other is the Co(1)−Co(3) and Co(1)−Co(4) interactions [N = 2, cis-O(Ac), Figure 1]. Analogous results were obtained for the Co(IV) data (blue line in Figure 2) and the Co(IV) localized DFT geometry (Table S1 and Figure S1, SI). Relative to **1**, most metal−ligand bond distances contract in Co(IV) (blue lines, Figure 3), reflecting increased Z_{eff}. The cis-N(py) Co−Co distance decreases slightly from 2.85 to 2.82 Å, while the 2-fold degenerate Co−Co [cis-O(Ac)] decreases from 2.73 to 2.68 Å. Additionally, the Co−O(oxo) bond distances

contract from 1.87 to 1.82 Å, and the Co−O(AcO) bond lengths decrease from 1.96 to 1.91 Å. The Co−N(py) distance increases from 1.93 to 2.00 Å. Thus, the EXAFS data of Co(IV) can be described and modeled using the Co(IV) distorted DFT geometry. Additionally, the relative intensity ratio of the first and second coordination shells in the *R*-space spectra of Co_4O_4 are more similar to ultrathin CoP_i[7] films than thicker CoP_i films and amorphous cobalt oxides,[72] reflecting the lower number of Co−Co vectors per Co ion in the surface CoP_i sites than in the bulk CoP_i.[7]

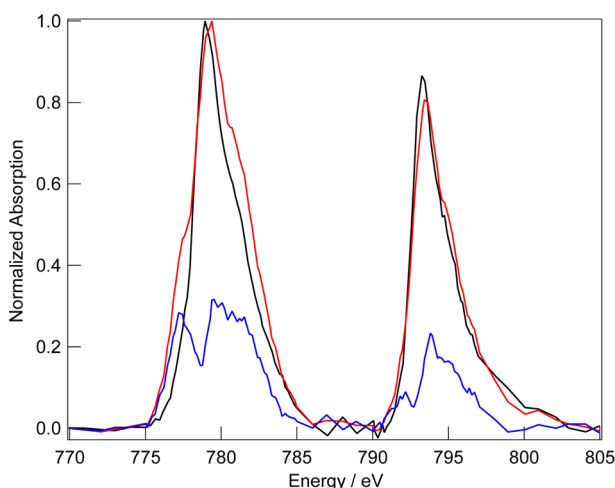**Co L-Edge XAS.** The L-edge XAS data are given in Figure 4, normalized to unity at ∼780 eV. Two intense features are

Figure 4. Co L-edge XAS: **1** (black line), **2** (red line), and Co(IV) (blue line).

observed at ∼779 and 793 eV for **1**. The L-edge excites Co 2p core electrons to unoccupied 3d orbitals [e.g., $2p^63d^6 \rightarrow 2p^53d^7$ for Co(III)]. Two features, split by ∼14 eV, are observed due to 2p core-hole spin−orbit coupling (SOC), resulting in a lower-energy L_3 ($J = \frac{3}{2}$) and higher-energy L_2 ($J = \frac{1}{2}$) edge. Upon oxidation, the L_3- and L_2-edges of **2** shift to higher energy (∼0.5 and ∼0.2 eV, respectively). Note that the energy positions are not necessarily reflective of energy differences between states without the 2p core-hole and are therefore also sensitive to the strong 2p/3d interactions. The L_3-edge of **2** broadens considerably, with growth of distinct shoulders on the lower and higher energy sides. The Co(IV) spectrum (Figure 4, blue line), obtained as for the Co K-edge, shows splitting on the L_3- and L_2-edges with peak maxima at ∼777.4 and 779.5 eV ($\Delta \cong 2.1$ eV) and ∼792.2 and 794 eV ($\Delta \cong 1.8$ eV), respectively. As in the K-edge XAS, the overall spectral shape of the L-edge is similar to isoelectronic, low-spin d^5 Fe(III).[73−75]

Co 1s3p Resonant Inelastic X-ray Scattering. $K\beta$ emission involves the decay of 3p electrons to a 1s core-hole formed from ionization or promotion to unoccupied bound states on the X-ray absorbing atom. The 3p/3d electron interactions are strong, thus making $K\beta$ sensitive to the electronic structure of the metal, especially spin state.[76] The Co $K\beta$ emission spectra obtained using 7730 eV excitation are given in Figure S2 (SI) and are consistent with an $S = 0$ to $S = \frac{1}{2}$ conversion.[76]

The Co 1s3p ($K\beta$) RIXS data were collected at Sector 27 at the Advanced Photon Source using the MERIX instrument.[77] RIXS planes for **1** and **2** are given in Figure 5. The data are normalized to the 1s → 3d pre-edge intensities (Figure 2).
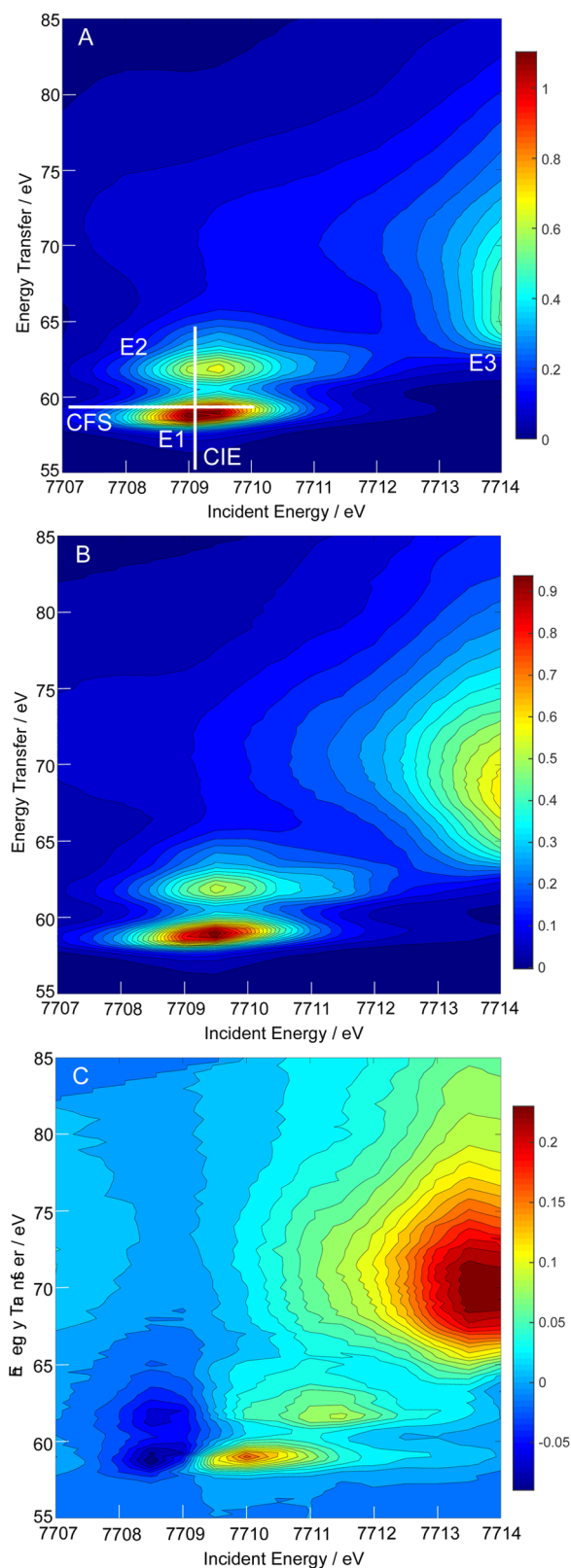

Figure 5. 1s3p RIXS planes for (A) **1**, (B) **2**, and (C) Co(IV) [e.g., **2** − ($\frac{3}{4}$)**1**].

Figure S3 (SI) provides a schematic description of the overall RIXS process. Briefly, the two-dimensional plots have incident energy (Ω) and energy transfer ($\Omega - \omega$) axes. $K\beta$ RIXS involves exciting at Co K-edge energies (e.g., 1s → 3d/4p
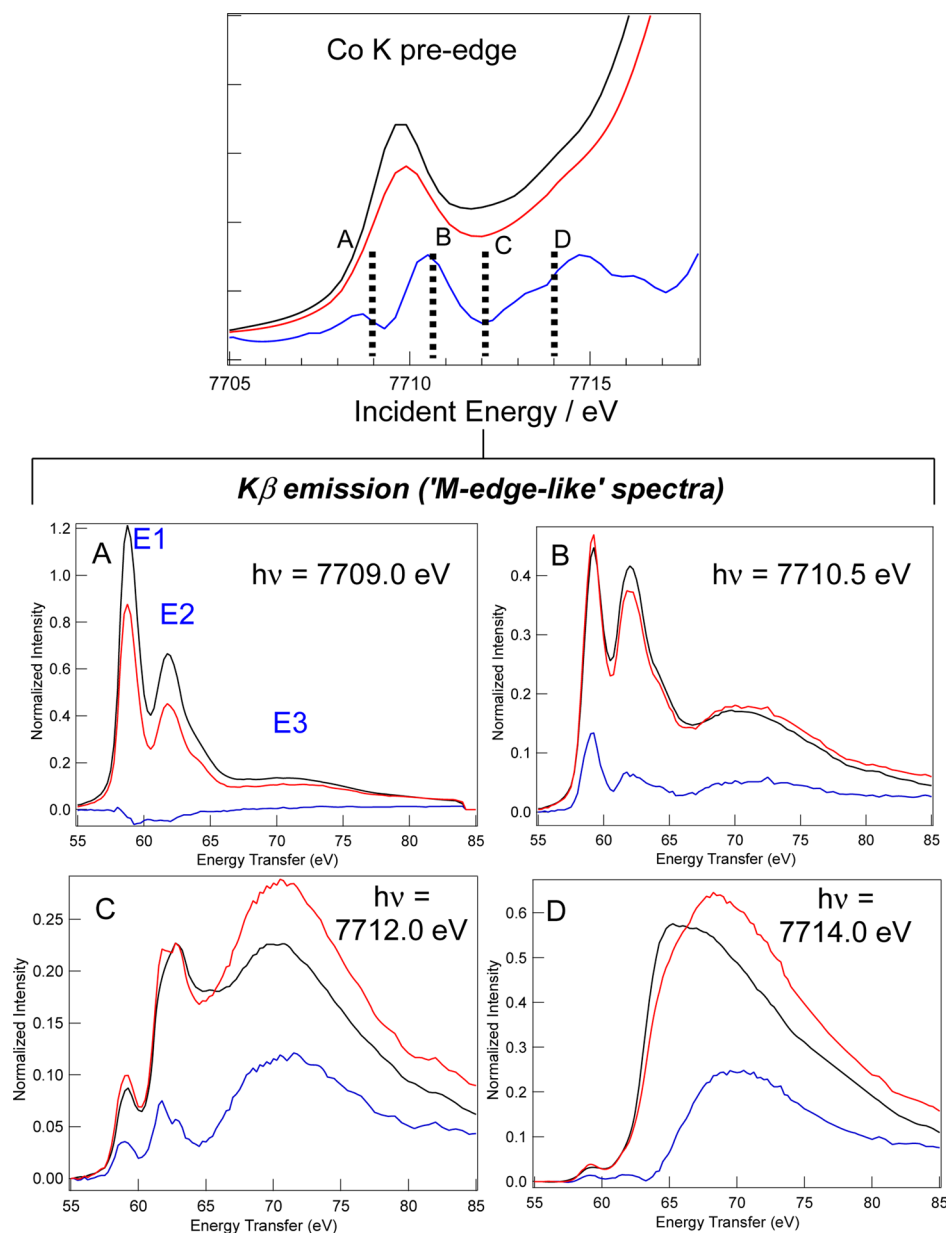
Figure 6. Constant incident energy cuts of the 1s3p RIXS planes: **1** (black line), **2** (red line), and Co(IV) (blue line).

transitions) and monitoring the resulting 3p → 1s Kβ emission. Taking a difference between the incident and fluorescence energies ($\Omega - \omega$) allows the data to be plotted with an energy transfer (ET) axis. The RIXS plane is constructed by measuring the Kβ emission as a function of incident energy. The two-photon process from initial to final state (gray dashed arrow in Figure S3, SI) corresponds roughly to a 3p → 3d absorption process (i.e., M-edge) located at ~60 eV for Co. However, the RIXS data can vary significantly from M/L-edge absorption due to different selection rules for the single-photon absorption (XAS) and two-photon RIXS process.[15,76]

The RIXS plane for **1** (Figure 5A) shows a strong feature centered at the 1s → 3d pre-edge energy (~7709.5 eV, Figure 2). The features in the RIXS plane are broadened in the incident energy axis from the 1s core-hole lifetime and along the ET axis from the 3p core-hole lifetime, resulting in anisotropy about the diagonal. Within the pre-edge region, **1** exhibits two sharper, strong ET features with energies of

~58.75 (E1) and 61.75 (E2) eV; a broader feature is observed at ~71 eV (E3), which increases in intensity as the incident energy increases, becoming dominant at incident energies greater than ~7712 eV.

The overall appearance of the RIXS plane of **2** appears similar to that of **1**, but several differences are observed. In the pre-edge, **2** also exhibits two sharp features with ET maxima at ~59.00 (E1) and 62.00 (E2) eV; the broader feature, E3, at ~71 eV is also present for **2** and increases in intensity with increasing incident energy. The relative intensity of E3 is greater for **2** than for **1**.

Similar to the difference spectra described above, a difference RIXS spectrum (Figure 5C) clearly displays the spectral contributions that derive from formation of Co(IV) in Co₄O₄. Spectral intensity is observed at incident energies >7709.5 eV, with larger differences observed from 7712 to 7714 eV (Figure 5C). These features appear in the energy regions labeled M/M in the Co(IV) K-edge XAS (Figure 2). A small

amount of residual negative intensity is observed in the Co(IV) RIXS plane at energies less than 7709 eV, which is likely due to the very low signal intensity, large Co(III) background, and the approximate nature of the overall difference spectrum, as discussed above. Generally, the sharpness of the E1 and E2 features is consistent with localized, quadrupole excitations to 3d-based intermediate states. Interestingly, the resonantly excited E3 feature is very broad and provides strong evidence that it derives from delocalized intermediate state(s) that involve oxygen-mediated M/M bonding in Co_4O_4,[69] indicating that it is a direct probe of M/M interactions and oxidation state in clusters and anodes. In the following section, the RIXS data are further analyzed by taking slices or cuts along the x- and y-axes of Figure 5.

Constant Final State Cuts. Constant final state (CFS) cuts are slices in the RIXS plane through the ET axis (labeled CFS in Figure 5A). The CFS cuts provide a spectroscopic probe that fixes the final state $[\Omega - \omega, 3p^53d^{7(6)}$ for Co(III) (Co(IV))] and scans the intermediate states $(1s^13d^{7(6)})$ that decay to that particular final state, thus providing an effective probe of all 1s K-edge resonances that decay into a fixed final state.

A series of CFS cuts for **1** and **2** in the 7707−7714 eV region are shown in Figure S4 (SI). For these, CFS cuts are shown through E1 or E2 features, as labeled in Figure 5A. Representative CFS cuts for **1**, **2**, and Co(IV) at ET values of 59 (E1) and 63 (E2) eV are given in Figure S4, parts E and F (SI), respectively. The cuts through E1 result in sharp pre-edge-like features centered around 7709.5 eV. The Co(IV) spectrum (blue line, Figure S4E, SI) shows increased intensity at incident energies of ∼7710 eV, consistent with the sharp feature observed in the Co K-pre-edge (Figure 2). CFS cuts taken through E2 are given in Figure S4F (SI). Additional intensity is now observed at incident energies >7710 eV for both **1** and **2**. The Co(IV) spectrum taken through E2 now shows additional intensity across the 7710−7714 eV region. Thus, it appears that difference CFS cuts allow for Co(IV) contributions in the pre-edge region to be distinguished, and the intensity distribution is dependent on the specific final states that are selected (e.g., via slices in E1 vs E2). These cuts are also shifted toward higher incident energies than for Co(III) due to the higher Z_{eff} of Co(IV), similar to the Co(IV) K-pre-edge in Figure 2.

Constant Incident Energy Cuts. Constant incident energy cuts, labeled CIE in Figure 5A, are taken through the incident energy axis. These $K\beta$ emission spectra are representative of "M-edge like" spectra, with ETs around 60 eV for Co (dotted gray arrow in Figure S3, SI). The CIE cuts hold the $1s^13d^{n+1}$ intermediate state (Ω) fixed while the final states $(\Omega - \omega)$ are varied/scanned. This indicates what final states can be reached via a particular 1s resonance.

CIE cuts across the RIXS planes of **1** and **2** are given in Figure S5 (SI). Some representative CIE cuts are given in Figure 6, which also shows the CIE resonance profiling behavior. Respective excitation energies are indicated within the K-pre-edge, and E1, E2, and E3 are labeled in Figure 6A. The CIE cuts are strongly excitation energy dependent, with E1 and E2 being resonantly excited in the K-pre-edge features involving quadrupolar 1s → 3d excitation. E3 is resonantly excited at energies >7712 eV. Splitting/structure is evident for E2.

Co(IV) CIE cuts (Figure 6, blue line) grow in at excitation energies greater than ∼7709.5 eV and increase with increasing excitation energy, indicating resonant excitation. This interpretation is consistent with the above observations that Co(IV) contributes strongly at pre-edge energies higher than Co(III).

However, the low-energy region of the pre-edge does not resolve specific emission spectral features associated with Co(IV).

Given the large differences observed in the ∼7712 eV pre-edge region in the Co K-edge and $K\beta$ RIXS, selective integrated spectra of Co(III)- and Co(IV)-based emission have been obtained by integrating the emission intensity through the 7112−7114 eV region (Figure 7). The data are highly sensitive
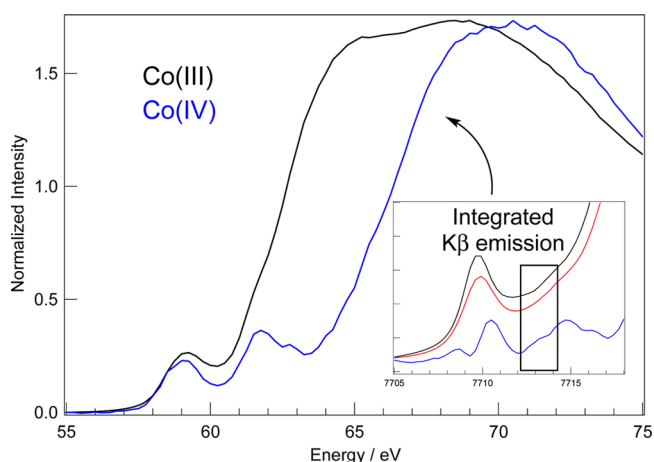

Figure 7. Integrated constant incident energy cuts of the 1s3p RIXS planes (sum of $K\beta$ emission in the 7112−7114 eV region is shown as an inset) of Co(III) in **1** (black) and Co(IV) in **2** (blue). Data are normalized for comparison.

to oxidation state. In particular, the lower-energy features (∼60−63 eV) show variations in intensity distribution, and the higher-energy region is strongly blue-shifted (∼3 eV) and shows differences in shape and structure. These data appear to represent a powerful probe of different oxidation states in high-valent, delocalized MV species.

In summary, the RIXS planes involve rich, oxidation state sensitive spectral features. E1, E2, and E3 are observed for **1**, **2**, and the difference spectrum obtained for Co(IV). While the absolute energies of E1 and E2 do not appear to be sensitive to oxidation state, intensity differences are observed in the Co(IV) spectra [Figures S5 (SI) and 6] with especially notable differences in splitting observed in the E2 energy region. E3 appears most sensitive to oxidation state. *Importantly, these spectroscopic data provide direct complementary probes of Co(IV) and M/M interactions (see below).*

Electronic Structure Calculations. Co_4O_4 Ground State. Several computational studies have explored mechanisms of water oxidation by Co_4O_4 cubanes with various ligand sets.[41,45,47,78,79] The majority employed the B3LYP functional [or a variation with 15% Hartree−Fock (HF) exchange] though one investigation used the PBE0 functional (25% HF exchange) to describe the spin delocalization over the cubane.[52] A computational goal was to evaluate the covalency of the ligand−metal bonds of the Co_4O_4 cubane and the oxidation potential as related to the experimental X-ray spectral data. Both of these experimental observables, covalency and oxidation potential, will be sensitive to the amount of HF exchange in the exchange−correlation functional. Several benchmarking calculations were therefore performed; full computational benchmarking results are given in the Supporting Information (see Tables S3−S5, SI). Briefly, the ground state of **2**, as determined by EPR measurements at 10

K, is mixed-valent and fully delocalized [i.e., 4Co(~3.25)]. In this context, the localized electronic configuration [3Co(III)/Co(IV)] can be considered as an excited state. The energy separation between these states is sensitive to the amount of HF exchange.[80,81] Generally, delocalized MV ground states are favored using pure generalized gradient approximation (GGA) functionals (0% HF), which suffer from a self-interaction error;[81,82] increasing HF exchange will localize the ground state wave function. Accordingly, the localized wave function of Co_4O_4 becomes the ground state at values of HF exchange >15% (Table S3, SI). We find that values of 15% HF exchange or less are needed to reproduce the time-averaged delocalization as determined by EPR. The calculated oxidation potential [$E^0(1)$, obtained from the adiabatic ionization energies] of Co_4O_4 is also sensitive to HF exchange. The experimental oxidation potential $E^0(1)$ of Co_4O_4 is 0.94 V vs NHE in CH_3CN (Figure S7, SI), which involves one-electron oxidation of 4Co(III) to the delocalized Co(IV)-containing cluster. The calculated adiabatic ionization energy (IE) of Co_4O_4 is 5.41 eV, including CH_3CN solvation effects using the polarized continuum model (Table 2). $E^0(1)$ is calculated to be 0.97 V vs NHE in CH_3CN (Table 2: $E^0 = IE - 4.44$ eV) at 15% HF exchange. The calculated $E^0(1)$ is severely underestimated at values of HF <15% (Tables S4 and S5, SI); thus, 15% HF exchange was used for subsequent calculations.

Geometry-optimized bond distances of all models are given in Table S2 (SI). The neutral and localized structures can adequately reproduce the EXAFS data. The calculated Co(d) and oxo(p) characters for the t_{2g}- and e_g-based orbitals of the cubane are given in Tables 1 and S6 (SI) [Mulliken population analyses (MPAs)]. We focus on the singly unoccupied β molecular orbital (MO) [e.g., the β lowest-unoccupied MO (β-LUMO)], the t_{2g}-based RAMO of Co_4O_4. The contour of the β-LUMO for the delocalized wave function is shown in Figure

8A and is consistent with previous literature.[52] The Co(d) and oxo(p) characters for the delocalized t_{2g}-based ground state by
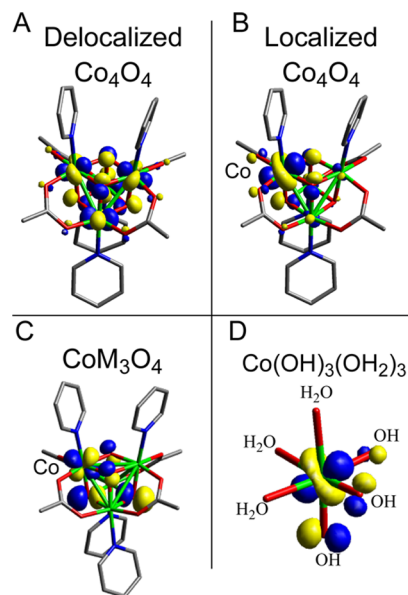

Figure 8. β-LUMOs for various versions and electronic structures of the cubane and a mononuclear model.

MPA are 63.8 and 25.6, respectively (Table 1, sums of all four Co or oxo atoms). The Mulliken spin densities reflect the β-LUMO and are calculated to be 0.16 and 0.09 for individual Co and O(oxo) atoms. This is qualitatively similar to previous literature;[52] the values here are slightly more Co-based due to the use of 15% HF exchange vs the 25% as previously used (see Tables S4 and S5 of SI for HF dependence on covalency).

The calculated MPA value of 63.8 total Co(d) character for the t_{2g}-based electron−hole indicates that the wave function is mainly Co-centered, partially ionic, and consistent with the relatively intense t_{2g} feature in the L-edge results above. However, to directly compare to experiment, the covalency of the localized wave function must also be considered. As mentioned, the localized wave function is actually the ground state at >15% HF; therefore, the localized, distorted geometry is obtained using a BP(20HF)86 functional. Subsequent single-point calculations were performed using 15% HF exchange as applied to the delocalized wave function, allowing for a direct comparison. The β-LUMO of the localized wave function (Figure 8B) clearly shows that the electron−hole is primarily localized to a single Co center. The total Co(d) and oxo(p) characters are 61.8 and 17.5 (23.5), relative to 63.8 and 25.6 (31.3) for the delocalized state [parenthetic values in Table 1 are total oxygen and nitrogen p-character, thus accounting for small contributions from OAc and N(py) ligands]. Note that the value of 61.8 Co(d) is for the ionized Co atom only. A small amount of "spectator Co" character (10.5) is present in the t_{2g}-based hole for the localized state. Including this amount in the total Co(d) character gives 72.3. Thus, the total Co(d) character of the localized wave function is 61.8 or 72.3, depending on the spectator amount. Given the importance of this value, a few points are noted. With HF exchange <15%, the Co(d) character of all four Co atoms is similar for delocalized (deloc) and localized (loc) geometries (Table S5, SI; deloc/loc 70.8/70.0, 69.0/68.4, and 66.7/67.2 for 0, 5, 10% HF, respectively). At values of HF >15%, the Co(d) character of

Table 1. Mulliken Population Analyses for the β-Based Unoccupied 3d MOs of Various Cubane Structures

	Co(d)	oxo(p)	OAc(p)	N(py)(p)
		Co_4O_4 (loc)[b]		
t_{2g} hole	61.8 (10.5)[a]	17.5	5.2	0.8
sum e_g	108.6 (12.7)[a]	53.8	14.2	6.2
		Co_4O_4 (deloc)[c,d]		
t_{2g} hole	63.8	25.6	4.6	1.1
sum e_g (/Co)	498.0 (124.5)	218.6 (48.3)	55.2 (13.8)	25.5 (6.4)
		$CoAl_3O_4$		
t_{2g} hole	46.1	47.5	2.2	0.4
sum e_g	117.5	53.2	21.0	0.4
		$CoGa_3O_4$		
t_{2g} hole	50.9	44.0	2.5	0.1
sum e_g	117.1	53.9	19.4	0.5
		$CoSc_3O_4$		
t_{2g} hole	57.6	33.8	4.6	0.0
sum e_g	113.0	48.0	18.5	0.2
	Co(d)	OH	H_2O	
		$Co(OH)_3(OH_2)_3$		
t_{2g} hole	63.5	35.0	0.4	
sum e_g	120.0	62.7	19.1	

[a]MPA characters of the other Co atoms for the localized wave function [formally Co(III)]. [b]Localized Co(IV). [c]Delocalized Co(IV). [d]Parenthetic values are total oxygen and nitrogen p-character.

all four Co atoms is slightly larger for the localized wave function (deloc/loc 63.8/72.3, 60.4/77.7, and 55.8/80.7, for 15, 20, and 25% HF, respectively). This "spectator Co" character derives from partial electron−hole delocalization, even in the localized, distorted geometry. Thus, small amounts of electron−hole delocalization in distorted geometries of the Co$_4$O$_4$ cluster cannot be ruled out. Given that the L-edge measurement involves excitation of core electrons on Co, we tend to favor values closer to ∼62% (i.e., no spectator Co). Future experiments, including perturbed Co$_4$O$_4$ structures, will help clarify this issue. Thus, delocalized and localized models appear to have similar amounts of Co d-character in their RAMOs (63.8 and 61.8, respectively), although, the localized state has less total ligand character than the delocalized state (23.5 and 31.3, respectively). This difference in ligand character occurs as localization decreases the effective number of oxo-ligands involved in bonding from four to three (see Figure 8, part A vs B), resulting in less oxo(p) character relative to delocalized Co(IV) (17.5 vs 25.6; a ratio of ∼3/4). This decreased oxo character in the localized state is distributed over "spectator Co" due to a small degree of partial delocalization. Note, the β-LUMO of a mononuclear model of a corner site of Co$_4$O$_4$ [e.g., Co(OH)$_3$(OH$_2$)$_3$] gives calculated Co(d) and O(p) characters of 63.5 and 35.0, respectively, similar to the values of 63.8 and 31.3 of the delocalized wave function (Figure 8D). *Thus, electron delocalization does not appear to decrease the amount of Co d-character in the RAMO, but an intrinsic amount of Co(IV)-based d-character is delocalized, which can change the distribution of the ligand character.* This is important when considering how electron−hole delocalization contributes to the redox properties of Co$_4$O$_4$, as is discussed below.

In addition to the Co(d) character of the RAMO, it is important to consider the distribution of the t$_{2g}$ hole over the t$_{2g}$-dπ orbitals. The t$_{2g}$-hole of delocalized Co$_4$O$_4$ has been described as d$_{xy}$ with partial d$_{xz}$/d$_{yz}$ mixing,[52] suggesting that the electron−hole undergoes partial localization in CoP$_i$. Indeed, the localized wave function calculated here takes on a different d-orbital mixing character (i.e., d$_{xz}$/d$_{yz}$/d$_{xy}$). As previously observed, the t$_{2g}$-hole of the delocalized state appears tilted or mixed d$_{xz}$/d$_{yz}$/d$_{xy}$ due to the canting of the Co(d)- and oxo(p)-orbitals to increase overlap (Figure 8A).[52] The degree of d-orbital mixing was not evaluated at that time, but it is calculated here to be ∼45% d$_{xz}$/d$_{yz}$ and ∼55% d$_{xy}$. This mixing changes to ∼56% d$_{xz/yz}$ and ∼44% d$_{xy}$ upon localization. *Thus, localization changes the nature of the d-orbital in the RAMO.* This is an important consequence for catalysis and redox properties, as different d-orbital characters allow for different orientations and metal−ligand bonding within the cubane core.

Oxidation Potential and Structural Perturbations of Co$_4$O$_4$: CoM$_3$O$_4$ (M = Al, Ga, and Sc). The RAMO of 2 is partially ionic, despite strong electron−hole delocalization over all Co and O(oxo) atoms. Given our experimental and computational considerations of localized vs delocalized wave functions, several structurally perturbed models of Co$_4$O$_4$ were targeted to gain insight into localized Co-based oxidation processes and to evaluate electron−hole delocalization contributions to redox chemistry. To do so, we evaluated the electronic structure of a single Co center within a CoM$_3$O$_4$ core, M = Al(III), Ga(III), or Sc(III), which were chosen because they are redox-inactive and conserve total charge on the cubane.

The optimized bond distances are given in Table S6 (SI), and the calculated E^0(1) values are given in Table 2. The E^0(1)

Table 2. Comparison between Experimental and Computational Oxidation Potentials

model	E^{0a}	$E^0(2)^a$	ΔE^b
Co$_4$O$_4$ (exp)	0.94	2.09	1.15
Co$_4$O$_4$ (calc)	0.97	2.15	1.18
CoAl$_3$O$_4$^{c}	0.64 (−0.33)	1.94 (−0.21)	1.30
CoGa$_3$O$_4$^{c}	0.72 (−0.25)	1.94 (−0.21)	1.22
CoSc$_3$O$_4$^{c}	0.86 (−0.11)	1.96 (−0.19)	1.10
Co(OH)$_3$(OH$_2$)$_3$^{c}	1.26 (0.29)		

^{a}Ionization energies converted to V vs NHE (IE − 4.44 eV). ^{b}E^0(2) − E^0(1). ^{c}Parenthetic values is the difference in calculated E^0 from that calculated for Co$_4$O$_4$.

values for the substituted cubanes were all lower than for Co$_4$O$_4$ by 100−300 mV (Table 2). This indicates that it is easier to form localized Co(IV) centers in CoM$_3$O$_4$ than it is to form delocalized Co(IV) in Co$_4$O$_4$ and that electron delocalization is not necessary for Co(IV) formation as opposed to other electronic factors, most important of which appears to be Co−O covalency. The ground-state Co(d) characters of the β-LUMOs of CoAl$_3$O$_4$, CoGa$_3$O$_4$, and CoSc$_3$O$_4$ are 46.1, 50.9, and 57.6, respectively; the oxo(p) characters are 47.5 (50.1), 44.0 (46.6), and 33.8 (38.4), respectively. The Co(d)- and oxo(p)-characters of CoM$_3$O$_4$ are significantly more covalent than Co$_4$O$_4$ (63.8/25.6), and the covalency decreases across the series Al > Ga > Sc, which inversely parallels the oxidation potentials (e.g., Al < Ga < Sc). The correlation between E^0(1) and covalency [total O(p) character from oxo and OAc ligands] is given in Figure 9 and
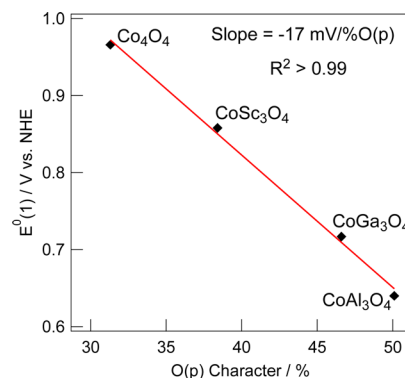

Figure 9. Linear dependence between oxidation potential and O(p) character.

exhibits an inverse linear relationship (R^2 > 0.99) with a slope of −17 mV/%O(p) character. The negative slope indicates that the oxidation potential lowers upon increasing covalency [e.g., ease of formation of Co(IV) is linearly related to covlency]. Correlations between covalency and oxidation potential have been observed in synthetic[83] and biological[84,85] FeS clusters and mononuclear, type I Cu proteins.[86] It is interesting to note that the slopes observed in those cases were ca. −8 mV/% S(p)[83,84] and −10 mV/%S(p),[86] on the order of what we observe in Figure 9. Thus, the different redox properties of Co$_4$O$_4$ and CoM$_3$O$_4$ are at least partially due to the difference in covalency of the RAMO. The origin of this difference is clear from the ground-state wave function [Figure 8C; this orbital is

representative of all three M(III) substitutions]. Upon substituting 3Co(III) with redox-inactive metals, the ground-state wave function, and thus the RAMO, rotates from mainly d_{xy} to pure d_{xz}/d_{yz}. Interestingly, this change in d-orbital character is of the same type observed for electron−hole localization within Co_4O_4. This switch forms highly covalent Co−oxo bonds due to greater orbital overlap of the oxygen p-orbitals with the metal d_{xz}/d_{yz} orbitals, thus stabilizing the oxidized over the reduced state and decreasing $E^0(1)$.

Computation shows that substituting 3Co(III) of a Co_4O_4 cubane core by 3Al(III), 3Ga(III), or 3Sc(III) strongly influences the redox properties of the M_4O_4 topology. Co(IV) formation can become more favorable at localized, mononuclear sites rather than a delocalized Co_4O_4 cluster. For similar structures with the same ground state, $E^0(1)$, and thus formation of Co(IV), appears to be linearly related to the extent of metal−oxygen covalency. The inductive influence[87] of Al(III)/Ga(III)/Sc(III)−oxo bonding on Co(IV)−oxo bonding can tune covalency and hence $E^0(1)$ over hundreds of millivolts (Figure 9).

■ DISCUSSION

The formation of Co(IV) species is critical to the activity of cobalt-based homogeneous and heterogeneous OECs.[31,41,47] In comparing molecular Co_4O_4 cubanes to the catenated Co_4O_4 cubane structure of heterogeneous CoP_i, the hole equivalents in the form of Co(IV) are "stored" within the cubane core. The Co(IV) redox level is highly oxidizing and thus difficult to characterize. Whereas EPR measurements have shown the Co(IV) hole equivalents to be delocalized within the cubane cluster, X-ray spectroscopies have the potential to "look inside" this apparent delocalization owing to the many orders of magnitude faster detection of this method. Accordingly, X-ray spectroscopy can directly probe and define the precise nature of the formal Co(IV) oxidation state as well as its bonding with oxygen and with neighboring metals within the cubane core. Such analysis of the Co(IV) state is facilitated by its correspondence to isoelectronic systems that have benefited from rigorous spectroscopic characterization.

Co K- and L-Edge Spectral Features. Low-spin Co(III) (t_{2g}^6) and Co(IV) (t_{2g}^5) are isoelectronic to Fe(II) and Fe(III), respectively. The K-pre-edge and the L-edge provide a direct probe of the 3d manifold through 1s and 2p excitations to unoccupied 3d orbitals, respectively. These spectroscopic methods provide a high degree of complementarity, as they probe different final states $(1s^13d^{n+1}$ and $2p^53d^{n+1})$ and have different selection rules (quadrupole for 1s → 3d and dipole for 2p → 3d). The K-pre-edge features provide information on geometric and electronic structure through the energy splittings and intensity distributions. The former are reflective of the ligand field strength. In a centrosymmetric complex, pre-edge transitions exhibit quadrupole intensity; however, distortions eliminating inversion symmetry give rise to 4p mixing over the many-electron final states, which gives partial dipole character to the pre-edge, increasing intensity. The energy splittings and intensities can also be affected by covalency. Westre et al. have provided a rigorous interpretation of iron K-pre-edge data in terms of the excited state d^{n+1} electronic configurations.[67] While the d^{n+1} excited electronic configurations should be coupled to the 1s core-hole, it is symmetric (a_{1g}) and will not affect the overall symmetry of the final state. The presence of the core-hole does not change the relative energies of the final states but can reduce 10Dq by ∼80% relative to the ground state by

decreasing Z_{eff} on the metal.[67] Thus, parent d^{n+1} states are referred to, and the analysis provides a direct correlation to the strong-field many-electron excited states of the Tanabe−Sugano matrices.[88] The ground-state configuration of low-spin Co(III) is $(t_{2g})^6$; excitation of a 1s core electron results in a $(t_{2g})^6(e_g)^1$ excited configuration, which gives rise to a ^2E_g excited state and a single pre-edge feature, consistent with the K-pre-edge of **1** (Figure 2). Excitation of a 1s core electron in Co(IV) can result in either $(t_{2g})^6$ or $(t_{2g})^5(e_g)^1$ excited configurations. The $(t_{2g})^6$ excited configuration gives rise to the $^1A_{1g}$ final state, and coupling the electrons in $(t_{2g})^5(e_g)^1$ gives rise to $^1T_{1g}$, $^3T_{1g}$, $^1T_{2g}$, and $^3T_{2g}$ final states. The intensity ratio of the pre-edge features from excitations to the t_{2g}:e_g-based holes is 1:4 in the absence of spin−orbit coupling, electron−electron repulsion, and covalency. The K-pre-edge obtained here for Co(IV) exhibits two transitions split by ∼1.9 eV with an ∼1:4 intensity ratio. The relative energies of the many-electron excited states that contribute to the pre-edge can be estimated using the d^6 Tanabe−Sugano matrices. Using the covalency-scaled free ion B value of 1000 cm^{-1}, excited 10Dq = 21 500 cm^{-1}, and $C = 4B$, the energies of $^3T_{1g}$, $^3T_{2g}$, $^1T_{1g}$, and $^1T_{2g}$ final states are calculated to be 1.20, 2.15, 2.20, and 4.15 eV, respectively. These energy values, combined with an equal intensity weighting, reproduce the 1.9 eV energy splitting between the low- and high-energy Co(IV) pre-edge features (blue line in Figure 2). Only the $^3T_{1g}$, $^3T_{2g}$, and $^1T_{1g}$ states likely contribute to the intensity of the higher energy pre-edge feature, while the $^1T_{2g}$ state is ∼4.2 eV higher in energy and likely contributes in the low-energy region of the broad ∼7114 eV feature. We note the energy splitting of Co(IV) in Co_4O_4 is closer to $[Fe(prpep)_2](ClO_4)$ (∼1.7 eV) and is significantly less than $K_3[Fe(CN)_6]$ (∼3.2 eV). From the pre-edge splitting and intensity distribution, the ground state 10Dq of Co(IV) is estimated to be ∼26 900 cm^{-1}. This agrees well with the value of ∼27 000 cm^{-1}, determined from fits to magnetism and EPR data of $La_{1.5}Sr_{0.5}Li_{0.5}Co_{0.5}O_4$ (vide infra).[89]

As in the K-pre-edge, the Co(IV) L-edge spectrum in Figure 4 bears significant resemblance to low-spin Fe(III). Generally, 2p/3d interactions and the 2p spin−orbit spitting dominate the L-edge final states. Therefore, the overall spectral shape, energies, and intensities can be influenced by a number of interactions, including the amount of 3d character (i.e., charge transfer effects), crystal field splitting, and distortion from O_h. For low-spin d^5 systems, the L_3 feature exhibits splitting and multiplet structure, where the lower-energy component of the L_3-edge is largely associated with absorption to the t_{2g} hole $[^1A_{1g}, (t_{2g})^6$ final state].[75,90] Analogous to low-spin Fe(III), Co(IV) in Co_4O_4 exhibits this feature, which is energetically well-separated from the higher-energy packet; in some Fe(III) cases, this feature has been shown to be pure π in nature (i.e., only t_{2g} intensity). The higher-energy L_3 feature primarily arises from transitions to the e_g holes and has dominantly σ character with some π mixing, but exhibits strong multiplet character. Given the dipole-allowed nature of the L-edge, the total intensity is related to the amount of d-character or covalency. Detailed multiplet analyses, including wave function projection methods, can give a great deal of information content, including differential orbital covalencies, and are the subject of a future study on a series of perturbed cubanes and Co(IV) ground states. Thus, the L-edge data can provide a direct comparison to literature data where structures are also known and provide an important benchmark and reference for future studies involving

perturbed versions of Co_4O_4, Co clusters, and oxides containing Co(IV).

Comparing Molecular and Heterogeneous Systems. The valency of perovskites can be controlled via Sr substitution.[91] The Co(IV) L-edge spectrum of Co_4O_4 is compared to $La_{1.8}Sr_{0.2}Li_{0.5}Co_{0.5}O_4$[92] in Figure 10 (normalized
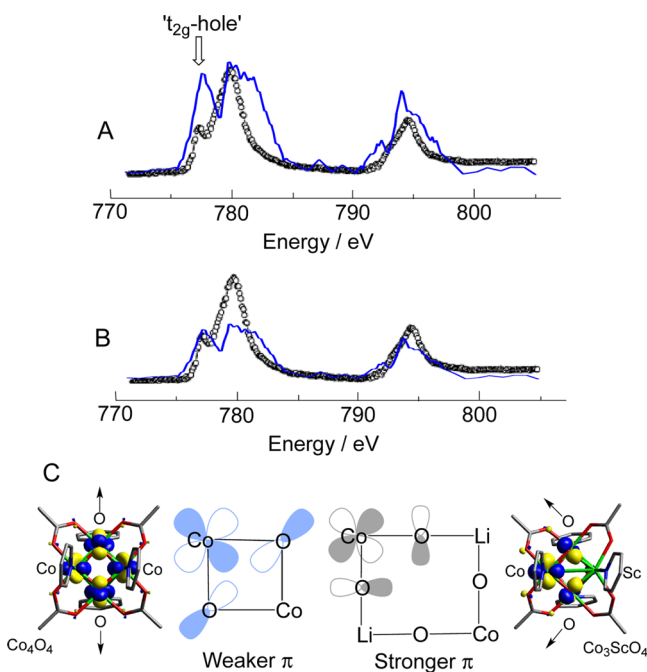

Figure 10. L-edge overlay between Co_4O_4 and $La_{1.8}Sr_{0.2}Li_{0.5}Co_{0.5}O_4$. Data are normalized to the e_g (A) and t_{2g} (B) features for comparison. The Co(IV) spectrum obtained here (blue line) is compared to the Co(IV) spectrum of $La_{1.8}Sr_{0.2}Li_{0.5}Co_{0.5}O_4$ obtained in ref 92. (C) Qualitative ground-state orbital overlaps for Co_4O_4 (blue, left center) and $La_{1.8}Sr_{0.2}Li_{0.5}Co_{0.5}O_4$ (gray, right center), as derived from EPR, are compared to DFT-derived β-LUMOs of Co_4O_4 (left) and Co_3ScO_4 (right).

to the e_g and t_{2g} features in parts A and B, respectively); differences in the intensity distribution patterns are observed in either case. Most striking is the relative intensities of the t_{2g} features, which are significantly less pronounced in $La_{1.8}Sr_{0.2}Li_{0.5}Co_{0.5}O_4$, and the increased intensity in the higher-energy region of the L_3 e_g feature for Co_4O_4. Additionally, the L_2 t_{2g} feature observed for Co_4O_4 is very weak or not present in $La_{1.8}Sr_{0.2}Li_{0.5}Co_{0.5}O_4$. This can reflect low overall t_{2g} intensity, even for the L_3-edge in $La_{1.8}Sr_{0.2}Li_{0.5}Co_{0.5}O_4$. However, the intensity of this feature is also related to symmetry-lowering distortions from O_h, such as structural or dynamic Jahn−Teller effects.[90,93,94] Additional insight can be gained from comparisons to other spectroscopic methods that do not involve core-hole formation.

Previous analyses of the $La_{2-x}Sr_xLi_{0.5}Co_{0.5}O_4$ magnetism and EPR data required significantly covalent Co−O bonding, as reflected by the low Stevens' orbital reduction factor (k)[95] of ∼0.65 (values <1 indicate covalent mixing).[89,96] It was also noted that Li−O bond linkages of neighboring octahedra (see Figure 10, bottom right) may provide an additional means of increasing the covalency of Co−O bonds.[89] The EPR g-values of $La_{1.5}Sr_{0.5}Li_{0.5}Co_{0.5}O_4$ are $2.32 \leq g_\perp \leq 2.55$, $g_\parallel \leq 0.85$ (calcd $g_\perp = 2.32$, $g_\parallel = 0.80$)[89] and 2.442, 2.237, and 0.8 for $La_{1.8}Sr_{0.2}Co_{0.5}O_4$,[92] which are notably different than those

of $[Co_4O_4(OAc)_2(py)_4]^+$ (2.3335, 2.3245, 2.0608).[53] These differences in g-values reflect different ground states, orbital orientations, and covalencies. The theory of Griffith[97] and Taylor[98] has been applied extensively to low-spin Fe(III) heme and nonheme centers to define the ground-state wave function, where $\sum g_i^2 = 16$ for a pure $d_{xy}^2 d_{xz/yz}^3$ ground state and $\sum g_i^2 = 12$ for a pure $d_{xy}^1 d_{xz/yz}^4$ ground state. Values of 15.1 and 11.6 are obtained for Co_4O_4 and $La_{1.8}Sr_{0.2}Li_{0.5}Co_{0.5}O_4$, respectively. The higher value for Co_4O_4 suggests a mixed $d_{xz/yz/xy}$ ground state, consistent with previous suggestions[52] and the DFT results obtained here. The low value for $La_{1.8}Sr_{0.2}Li_{0.5}Co_{0.5}O_4$ suggests a pure d_{xy} Co(IV) ground state.

Molecular orbital considerations gleaned from EPR and DFT calculations for Co_4O_4[52] and $La_{2-x}Sr_xLi_{0.5}Co_{0.5}O_4$[89] lead to the picture observed in Figure 10C (left and right center, respectively). The $d\pi$ orbital bisects the Co−O bonds in both structures; however, while the oxo-ligand p-orbitals are purely π-interacting with the metal 3d orbital in $La_{2-x}Sr_xLi_{0.5}Co_{0.5}O_4$ (Figure 10C, right center), they are misaligned and rotated off-axis in Co_4O_4 (Figure 10, left center). This misalignment derives from electron−hole delocalization in Co_4O_4, which directs the metal d-orbitals into the center of the diamond core to increase M/M coupling. Thus, the situation exists where maximizing delocalization misaligns the Co d- and oxo p-orbitals, decreasing the covalency of Co−O bonds. A recent study has found increased OER activity in structurally distorted $La_{1-x}Sr_xCo_3$ perovskites, rationalized by increased Co−O covalency and conductivity.[99] Our results here have showed that increased covalency decreases $E^0(1)$, driving Co(IV) formation, which will also enhance OER activity and conductivity. Future mechanistic studies will be necessary to better correlate and compare molecular and solid-state OER catalysis. Thus, knowledge of the 3d-orbital character is of limited importance if the resulting orientation with oxo p-orbitals is not known. The orientation clearly has a strong influence on the nature of the covalency and antibonding contributions to redox potentials. In testament, we can converge a wave function in a Co_3ScO_4 model that rotates the cubane oxo p-orbitals, resulting in orbital overlaps similar to those suggested for $La_{1.8}Sr_{0.2}Li_{0.5}Co_{0.5}O_4$. The β-LUMO is given in Figure 10C (far right) and can be directly compared to Co_4O_4 (far left). The arrows indicate the orientation of the oxo p-orbitals. In this model, Co(IV) formation takes place on a single Co center in Co_3ScO_4, with an $E^0(1)$ of 0.81 V vs NHE, 160 mV lower than that of Co_4O_4 (0.97 V).

Spectral Probes of Metal−Metal Interactions in Co_4O_4. Besides ligand−metal covalency, M/M interactions contribute strongly to the electronic structures and properties of MV species. Our combined K-edge and RIXS data provide a direct spectroscopic probe of both Co(IV) formation and M/M interactions in Co_4O_4. The Co K-edge exhibits a feature at ∼5 eV higher in energy than the pre-edge (labeled M/M in Figure 2), which is present for Co(III) in **1** and Co(IV) in **2**, appearing slightly more intense in the latter. Spectral features occur at this relative energy position for low-spin mononuclear compounds such as $K_3[Fe(III)(CN)_6]$[67,90] and $K_3[Co(III)(CN)_6]$.[100] Yet these spectral features have been assigned to transitions to low-lying π^* orbitals of CN^-, and they have been used as probes of backbonding. Interestingly, whereas this feature is not present in low-spin $Co(acac)_3$, it is observed in low-spin Co(III)-containing $LiCoO_2$, $AgCoO_2$, $EuCoO_3$, and $LaCoO_3$,[70] and it has been assigned to a dipolar transition to low-lying orbitals

with significant M/M character [suggested to be a formally $M(1s^13d^n)M'(1s^23d^{n+1})$ XAS final state[69−71]]. This is based on several observations: (i) the intensity in the K-edge feature correlates with the Co−O−Co angle of edge-facing (for Li and Ag) and corner-facing (for Eu and La) octahedra, with the greatest intensity observed for structures with wider Co−O−Co angles (e.g., 152.9° for $EuCoO_3$ and 94.2° for $LiCoO_2$); (ii) the angular dependence of the K-edge intensity in a single crystal, and (iii) the dispersion (spectral broadness) of the resulting emission features obtained in RIXS measurements (i.e., emission features are broadened or elongated for dipolar and sharp for quadrupolar). The data presented here are specific to observation iii; for instance, resonant excitation into the ~7714 eV feature results in a dominant, broad feature, E3, which evolves and is enhanced in Figure 6, from part B to C to D. Additionally, E1 and E2 are sharp while E3 is broad, reflective of their quadrupole and dipole characters, respectively. E3 is also highly sensitive to oxidation state (Figures 6D and 7). This description of the quadrupolar and dipolar character observed in the XAS and RIXS data can also be described in terms of the amount of delocalization in the X-ray intermediate and final states. Specifically, excitation of the 1s/2p → 3d K-pre-edge (and L-edge absorption) results in data that reflect localized transitions on the Co(IV) and Co(III) X-ray absorbing/excited atom. However, the M/M feature can be assigned to a nonlocal 1s → 3d/4p transition that gains intensity through $M(4p)−O(2p)−M'(3d)$ hybridization and can result in a formal electronic configuration of $M(1s^13d^n)/M'(1s^23d^{n+1})$, where contributions can now arise from neighboring Co 3d orbitals.[70,71] Thus, in comparing resonant excitation into the local and nonlocal 1s → 3d/4p regions, local excitation results in a RIXS final state that is $M(1s^23p^53d^{n+1})$, which involves *intra*-atomic 3p/3d interactions. Conversely, nonlocal excitation can potentially result in RIXS final states with $M(1s^23p^53d^n)M'(1s^23p^63d^{n+1})$ character, which involves *inter*-atomic 3p/3d interactions.

It is interesting to note that, in $LiCoO_2$ (and other extended solids mentioned here), the local and nonlocal features are split by ~2−3 eV, which is significantly less than the splitting observed for Co_4O_4 (~5 eV). The energy splitting between these final states is thought to derive from differences in core-hole screening between the local and nonlocal excitations.[70,71,101] The 5 eV energy separation observed here implies a further perturbation of the relative energy of the nonlocal state relative to the local state, potentially through differences in relative core-hole screening in the molecular Co_4O_4 vs extended heterogeneous systems.

Thus, the combined XAS/RIXS data provide insight into the degree of M/M interactions and potentially electron−hole delocalization across Co_4O_4 through intensities and energy splittings. The XAS/RIXS data in the M/M region for Co_4O_4 will be further modeled in a future study using DFT and TDDFT calculations that will also evaluate the effect of the core-hole. These data can be directly compared to other clusters and cobalt oxide thin films, and the relative degrees of M/M interactions and charge delocalization should be able to be probed and quantified.

Electron−Hole Delocalization in Co_4O_4 and Comparisons to Heterometallic Cubane Clusters. It is important to consider that core-hole formation is considered to be instantaneous, with core-hole lifetimes varying from ~1−4 fs. This leads to a roughly 6 orders of magnitude decrease in the spectroscopic time-scale relative to EPR. Also, the core-hole

potential can strongly influence the valence electrons of the X-ray absorbing *and* neighboring O and Co atoms, and the electron density will respond on the ultrafast time scale to screen the core-hole. These factors can contribute to a more localized Co(IV) description relative to longer time scale spectroscopies, such as EPR. Core-hole screening is especially important to consider in photoemission measurements where a true core-hole is created (as opposed to X-ray absorption to bound states where the excited electron can also partially screen the core-hole potential). Indeed, distinct features for localized oxidation states have been observed in photoemission studies of class III mixed-valence species, such as the Creutz−Taube ion,[55,102] which arise from final state effects. Electronic absorption spectroscopy provides an additional method with ultrafast time scales ($\sim10^{-14}$ s) and can provide a direct correlation to the X-ray spectroscopic data. In this case, the core-hole is not present and therefore its effect on localization can be eliminated. In MV systems, the energy, intensity, and bandwidth of the intervalence charge transfer (IVCT) transition can be used to quantify electron−hole delocalization.[65] The room temperature electronic absorption spectra of **1** and **2** in the energy range of 400−3000 nm (25 000−3000 cm^{-1}) are given in Figure S8 (SI). Within this energy range, **1** exhibits weak features at ~600 nm (~16 670 cm^{-1}). Interestingly, **2** also exhibits absorption features at the same energy as **1**; however, an additional band, assignable to IVCT, grows in at ~4600 cm^{-1} upon oxidation to **2**. Bandwidth analysis indicates that **2** is a class II MV complex.

Electron−hole delocalization is thought to be a main factor for stabilizing Co(IV) in Co_4O_4. Certainly, a contribution from delocalization exists, as demonstrated by comparisons between the mononuclear corner site model and Co_4O_4. However, given that Co(IV) can be formed more easily at effectively mononuclear sites in perturbed cubane structures, other considerations such as covalency need to be considered. Electron delocalization may provide an electrostatic stabilization of the oxidized state over the reduced state, arising from distributing charge across multiple atoms of the cluster. This effect can be distinguished from the purely electronic effects of electron−hole delocalization, which we showed above can actually make it more difficult to form Co(IV). As an illustration, we calculated the relative energies of the reduced and oxidized states as a function of dielectric constant (Table S7, SI). In general, increasing the dielectric from 0 (gas phase) to ~36 (CH_3CN) significantly decreases the ionization energy for Co_4O_4 and CoM_3O_4 models (Table S7, SI) with the greatest stabilization observed for oxidized Co_4O_4 (Table S7, bolded, SI). This is due to delocalization of the charge over the cluster, which is considerably less for CoM_3O_4, as ionization is localized to mononuclear Co centers. While expected, this further illustrates that electron−hole delocalization does not necessarily intrinsically decrease $E^0(1)$ of Co_4O_4 but stabilizes the oxidized state over the reduced state by spreading charge across the cluster, and thus, additional effects are likely responsible for the stabilization of Co(IV) in Co_4O_4.

It is worth distinguishing time-averaged effective oxidation states (i.e., the result of fast hopping of electrons/holes between atoms, which may or may not be observed depending on the time scale of the measurement) from steady-state effective oxidation states due to orbital overlap and delocalization of states. These two pictures might correlate differently to catalysis. To a first approximation, the time-averaged, effective oxidation states are likely to be more ionic/less covalent,

whereas the latter picture necessitates strongly covalent ligand−metal bonding interactions. Thus, on the basis of the results here, the time-averaged oxidation states may potentially be more oxidizing than the highly covalent counterparts, but they may then be less effective at PCET charge transport, which suggests an important interplay between covalency and mixed-valency on, specifically, OER by cobalt-based films.

Lastly, though the CoM_3O_4 complexes used here for insight into localized oxidation processes are likely very difficult synthetic targets, they have proved useful for better understanding the effects of redox-inactive metal substitution in redox tuning of heterometallic clusters. Two key observations can be made: (1) substitution can simply tune the potential via an inductive effect, which varies the covalency of the metal−oxo bonds, and perhaps more interestingly, (2) they can completely change the identity of the RAMO by rotating/switching the ground-state wave function and thus bonding with the ligands. This first factor is related to a growing body of literature on heterometallic oxido complexes.[103−106] Recent studies demonstrated a linear dependence between E^0 and the pK_a of the redox-inactive metal ($\sim$100 mV/pK_a).[103] The trend was linked to the Lewis acidity of the substituted metal, which (in the absence of PCET) is an indirect measure of the first factor and is related to the results shown in Figure 9. Here, we provide a direct correlation between the inductive effect of metal substitution, which gives rise to the linear relationship between E^0 and metal−oxo covalency. However, both covalency and the ground state can change for redox-inactive metal substitutions depending on how they are incorporated. Additionally, switching the ground state can result in variable degrees of metal−metal interactions across the cluster (i.e., mixed-valency) based on the nature of the molecular orbital. This large variation in electronic structure can be utilized in the rational design and improvement of water-oxidizing catalysts, both homogeneous and heterogeneous.

Higher Oxidation States of Co_4O_4. As a final consideration, Co(V) states have been proposed for promoting Co_4O_4 reactivity.[41,47] A second oxidation, $E^0(2)$, of Co_4O_4 occurs at 2.09 V vs NHE in CH_3CN (Figure S7, SI), giving a $\Delta E^0(2-1)$ splitting of 1.15 V. $E^0(2)$ of Co_4O_4 is calculated here to be 2.15 V vs NHE, giving a $\Delta E^0(2-1)$ splitting of 1.18 V; the absolute and relative calculated values are in excellent agreement with experiment. Note that the second oxidation of the Co_4O_4 is preliminarily modeled as a $Co(III)_2Co(IV)_2$ triplet ($S = 1$), not a Co(V) localized state. Future studies are necessary to define the electronic structure of this state. We do note, however, that the calculated $E^0(2)$ values of $CoAl_3O_4$, $CoGa_3O_4$, and $CoSc_3O_4$ clusters (also triplets) are 1.94, 1.94, and 1.96 V vs NHE, respectively (Table 2), all of which are again less than Co_4O_4, suggesting that a formally Co(V) could be formed in CoM_3O_4 clusters.

Examining the ground-state wave functions (Figure S9, SI), we find that CoM_3O_4 effectively houses one of two redox equivalents within the oxo-bonding framework [e.g., effective ionization of O(2p)-based electrons or extremely covalent Co−oxo bonding for one of the unoccupied 3d-orbitals]. This can be viewed as a form of "redox-potential leveling" or "ligand noninnocence", potentially analogous to Co(III)−corroles, where one of two electron−holes necessary for water oxidation is delocalized within the corrole π-electron system.[107] Indeed, oxidation of oxo(2p) electrons has been proposed for Co and Ni oxides as well as $Li_{1.2}[Ni_{0.13}^{2+}Co_{0.13}^{3+}Mn_{0.54}^{4+}]O_2$.[108−112] Interestingly, in the latter example, holes generated upon oxidation are proposed to be effectively localized on Mn(IV)−O and not Co(IV)− or Ni(IV)−O bonds.[112] This form of redox noninnocence may allow perturbed clusters with effectively "mononuclear" sites to reach high formal oxidation states in a fashion similar to metal oxides.

In terms of oxidic metal OER catalysts, the formation of highly covalent surface exposed active sites within a covalent, mixed-valent matrix will lower Co-OEC Co(III/IV) redox potentials and drive OER activity by increasing Co(IV) content and by facilitating the regeneration of active sites via self-exchange proton-coupled electron transport. Increased covalency can also thus lower the necessary operating overpotential of the catalyst.

CONCLUSIONS

The formation of Co(IV) species is critical to the activity of cobalt-based homogeneous and heterogeneous OECs.[31,41,47] In comparing molecular Co_4O_4 cubanes to the catenated Co_4O_4 cubane structure of heterogeneous CoP_i, the hole equivalents in the form of Co(IV) are "stored" within the cubane core. Whereas EPR measurements have shown that these hole equivalents are delocalized within the cubane cluster, the XAS studies reported here indicate that the hole equivalents are localized on the much shorter time scale of an XAS experiment, suggesting that delocalization is thus achieved by a very fast hopping rate. Complementary X-ray spectroscopies have provided a direct probe of the Co(IV) d-orbital manifold in a Co_4O_4 cubane and have allowed for a comparison to isoelectronic d^5 molecular and heterogeneous species. Future studies are aimed at extending to 1s2p RIXS, which provide these data using hard X-rays. The combined K-edge and 1s3p RIXS data allow for the experimental "mapping" of Co(IV) contributions to the K-edge and RIXS planes in the presence of a spectroscopically active MV background. This sensitivity lends promise for applications to in situ measurements of cobalt oxides. Additionally, application of the XAS/RIXS combination has allowed spectral features to be identified that provide a direct handle on both Co(IV) and oxygen-mediated M/M interactions.

DFT calculations guided by the experiment indicate that electron−hole delocalization is not necessary for Co(IV) formation in clusters, and other factors such as covalency, antibonding, and inductive effects may be more important. In particular, maximizing electron−hole delocalization can result in a partial decrease in the covalency and orbital overlap of ligand−metal bonds and oppose the formation of high-valent states. Additionally, substituting redox-inactive metals results in a rotation of the ground-state wave function and increased ligand−metal covalency. This strongly helps drive the formation of Co(IV). For similar structures with the same ground state, $E^0(1)$, and thus formation of Co(IV), is shown to be linearly related to covalency, and the inductive influence of Al(III)/Ga(III)/Sc(III)−oxo bonding on Co(IV)−oxo bonding can tune covalency over a large range and thus $E^0(1)$ over hundreds of millivolts. Covalency-driven formation of high-valent species increases the number of active sites and facilitates regeneration.

ASSOCIATED CONTENT

Ⓢ Supporting Information

The Supporting Information is available free of charge on the ACS Publications website at DOI: 10.1021/jacs.6b04663.

Full experimental details, supporting tables and figures, and Cartesian coordinates of DFT-optimized geometries (PDF)

■ AUTHOR INFORMATION

Corresponding Authors

*dnocera@fas.harvard.edu

*lchen@anl.gov; l-chen@northwestern.edu

Notes

The authors declare no competing financial interest.

■ REFERENCES

(1) Lewis, N. S.; Nocera, D. G. *Proc. Natl. Acad. Sci. U. S. A.* **2006**, *103*, 15729.

(2) Cook, T. R.; Dogutan, D. K.; Reece, S. Y.; Surendranath, Y.; Teets, T. S.; Nocera, D. G. *Chem. Rev.* **2010**, *110*, 6474.

(3) Nocera, D. G. *Acc. Chem. Res.* **2012**, *45*, 767.

(4) Lewis, N. S.; Nocera, D. G. *Bridge* **2015**, *46*, 41.

(5) Kanan, M. W.; Nocera, D. G. *Science* **2008**, *321* (5892), 1072.

(6) Lutterman, D. A.; Surendranath, Y.; Nocera, D. G. *J. Am. Chem. Soc.* **2009**, *131*, 3838.

(7) Kanan, M. W.; Yano, J.; Surendranath, Y.; Dincă, M.; Yachandra, V. K.; Nocera, D. G. *J. Am. Chem. Soc.* **2010**, *132*, 13692.

(8) Dincă, M.; Surendranath, Y.; Nocera, D. G. *Proc. Natl. Acad. Sci. U. S. A.* **2010**, *107*, 10337.

(9) Trotochaud, L.; Young, S. L.; Ranney, J. K.; Boettcher, S. W. *J. Am. Chem. Soc.* **2014**, *136*, 6744.

(10) Hunter, B. M.; Blakemore, J. D.; Deimund, M.; Gray, H. B.; Winkler, J. R.; Müller, A. M. *J. Am. Chem. Soc.* **2014**, *136*, 13118.

(11) Smith, R. D. L.; Prévot, M. S.; Fagan, R. D.; Trudel, S.; Berlinguette, C. P. *J. Am. Chem. Soc.* **2013**, *135*, 11580.

(12) Song, F.; Hu, X. *J. Am. Chem. Soc.* **2014**, *136*, 16481.

(13) Qiu, Y.; Xin, L.; Li, W. *Langmuir* **2014**, *30*, 7893.

(14) Friebel, D.; Louie, M. W.; Bajdich, M.; Sanwald, K. E.; Cai, Y.; Wise, A. M.; Cheng, M.-J.; Sokaras, D.; Weng, T.-C.; Alonso-Mori, R.; Davis, R. C.; Bargar, J. R.; Nørskov, J. K.; Nilsson, A.; Bell, A. T. *J. Am. Chem. Soc.* **2015**, *137*, 1305.

(15) Lundberg, M.; Kroll, T.; DeBeer, S.; Bergmann, U.; Wilson, S. A.; Glatzel, P.; Nordlund, D.; Hedman, B.; Hodgson, K. O.; Solomon, E. I. *J. Am. Chem. Soc.* **2013**, *135*, 17121.

(16) Kroll, T.; Hadt, R. G.; Wilson, S. A.; Lundberg, M.; Yan, J. J.; Weng, T.-C.; Sokaras, D.; Alonso-Mori, R.; Casa, D.; Upton, M. H.; Hedman, B.; Hodgson, K. O.; Solomon, E. I. *J. Am. Chem. Soc.* **2014**, *136*, 18087.

(17) Kotani, A.; Shin, S. *Rev. Mod. Phys.* **2001**, *73*, 203.

(18) Ament, L. J. P.; van Veenendaal, M.; Devereaux, T. P.; Hill, J. P.; van den Brink, J. *Rev. Mod. Phys.* **2011**, *83*, 705.

(19) Li, C. W.; Ciston, J.; Kanan, M. W. *Nature* **2014**, *508*, 504.

(20) Feng, X.; Jiang, K.; Fan, S.; Kanan, M. W. *J. Am. Chem. Soc.* **2015**, *137*, 4606.

(21) Verdaguer-Casadevall, A.; Li, C. W.; Johansson, T. P.; Scott, S. B.; McKeown, J. T.; Kumar, M.; Stephens, I. E. L.; Kanan, M. W.; Chorkendorff, I. *J. Am. Chem. Soc.* **2015**, *137*, 9808.

(22) Petrie, J. R.; Cooper, V. R.; Freeland, J. W.; Meyer, T. L.; Zhang, Z.; Lutterman, D. A.; Lee, H. N. *J. Am. Chem. Soc.* **2016**, *138*, 2488.

(23) Woertink, J. S.; Smeets, P. J.; Groothaert, M. H.; Vance, M. A.; Sels, B. F.; Schoonheydt, R. A.; Solomon, E. I. *Proc. Natl. Acad. Sci. U. S. A.* **2009**, *106*, 18908.

(24) Vanelderen, P.; Hadt, R. G.; Smeets, P. J.; Solomon, E. I.; Schoonheydt, R. A.; Sels, B. F. *J. Catal.* **2011**, *284*, 157.

(25) Vanelderen, P.; Snyder, B. E. R.; Tsai, M.-L.; Hadt, R. G.; Vancauwenbergh, J.; Coussens, O.; Schoonheydt, R. A.; Sels, B. F.; Solomon, E. I. *J. Am. Chem. Soc.* **2015**, *137*, 6383.

(26) Gagliardi, C. J.; Vannucci, A. K.; Concepcion, J. J.; Chen, Z.; Meyer, T. J. *Energy Environ. Sci.* **2012**, *5*, 7704.

(27) Ullman, A. M.; Brodsky, C. N.; Li, N.; Zheng, S.-L.; Nocera, D. G. *J. Am. Chem. Soc.* **2016**, *138*, 4229.

(28) Ferreira, K. N.; Iverson, T. M.; Maghlaoui, K.; Barber, J.; Iwata, S. *Science* **2004**, *303*, 1831.

(29) Umena, Y.; Kawakami, K.; Shen, J.-R.; Kamiya, N. *Nature* **2011**, *473*, 55.

(30) Zhang, C.; Chen, C.; Dong, H.; Shen, J.-R.; Dau, H.; Zhao, J. *Science* **2015**, *348*, 690.

(31) Bediako, D. K.; Ullman, A. M.; Nocera, D. G. *Top. Curr. Chem.* **2015**, *371*, 173.

(32) Kanan, M. W.; Surendranath, Y.; Nocera, D. G. *Chem. Soc. Rev.* **2009**, *38*, 109.

(33) Beattie, J. K.; Hambley, T. W.; Klepetko, J. A.; Masters, A. F.; Turner, P. *Polyhedron* **1998**, *17*, 1343.

(34) Dimitrou, K.; Folting, K.; Streib, W. E.; Christou, G. *J. Am. Chem. Soc.* **1993**, *115*, 6432.

(35) Dimitrou, K.; Sun, J.-S.; Folting, K.; Christou, G. *Inorg. Chem.* **1995**, *34*, 4160.

(36) Dimitrou, K.; Brown, A. D.; Christou, G.; Concolino, T. E.; Rheingold, A. L. *Chem. Commun.* **2001**, 1284.

(37) Chakrabarty, R.; Bora, S. J.; Das, B. K. *Inorg. Chem.* **2007**, *46*, 9450.

(38) Sarmah, P.; Chakrabarty, R.; Phukan, P.; Das, B. K. *J. Mol. Catal. A: Chem.* **2007**, *268*, 36.

(39) Chakrabarty, R.; Sarmah, P.; Saha, B.; Chakravorty, S.; Das, B. K. *Inorg. Chem.* **2009**, *48*, 6371.

(40) Das, B. K.; Chakrabarty, R. *J. Chem. Sci.* **2011**, *123*, 163.

(41) Smith, P. F.; Hunt, L.; Laursen, A. B.; Sagar, V.; Kaushik, S.; Calvinho, K. U. D.; Marotta, G.; Mosconi, E.; De Angelis, F.; Dismukes, G. C. *J. Am. Chem. Soc.* **2015**, *137*, 15460.

(42) McCool, N. S.; Robinson, D. M.; Sheats, J. E.; Dismukes, G. C. *J. Am. Chem. Soc.* **2011**, *133*, 11446.

(43) La Ganga, G.; Puntoriero, F.; Campagna, S.; Bazzan, I.; Berardi, S.; Bonchio, M.; Sartorel, A.; Natali, M.; Scandola, F. *Faraday Discuss.* **2012**, *155*, 177.

(44) Berardi, S.; La Ganga, G.; Natali, M.; Bazzan, I.; Puntoriero, F.; Sartorel, A.; Scandola, F.; Campagna, S.; Bonchio, M. *J. Am. Chem. Soc.* **2012**, *134*, 11104.

(45) Li, X.; Siegbahn, P. E. M. *J. Am. Chem. Soc.* **2013**, *135*, 13804.

(46) Mattioli, G.; Giannozzi, P.; Amore Bonapasta, A.; Guidoni, L. *J. Am. Chem. Soc.* **2013**, *135*, 15353.

(47) Nguyen, A. I.; Ziegler, M. S.; Oña-Burgos, P.; Sturzbecher-Hohne, M.; Kim, W.; Bellone, D. E.; Tilley, T. D. *J. Am. Chem. Soc.* **2015**, *137*, 12865.

(48) Ullman, A. M.; Liu, Y.; Huynh, M.; Bediako, D. K.; Wang, H.; Anderson, B. L.; Powers, D. C.; Breen, J. J.; Abruña, H. D.; Nocera, D. G. *J. Am. Chem. Soc.* **2014**, *136*, 17681.

(49) Symes, M. D.; Lutterman, D. A.; Teets, T. S.; Anderson, B. L.; Breen, J. J.; Nocera, D. G. *ChemSusChem* **2013**, *6*, 65.

(50) Symes, M. D.; Surendranath, Y.; Lutterman, D. A.; Nocera, D. G. *J. Am. Chem. Soc.* **2011**, *133*, 5174.

(51) McAlpin, J. G.; Surendranath, Y.; Dinca, M.; Stich, T. A.; Stoian, S. A.; Casey, W. H.; Nocera, D. G.; Britt, R. D. *J. Am. Chem. Soc.* **2010**, *132*, 6882.

(52) McAlpin, J. G.; Stich, T. A.; Ohlin, C. A.; Surendranath, Y.; Nocera, D. G.; Casey, W. H.; Britt, R. D. *J. Am. Chem. Soc.* **2011**, *133*, 15444.

(53) Stich, T. A.; Krzystek, J.; Mercado, B. Q.; McAlpin, J. G.; Ohlin, C. A.; Olmstead, M. M.; Casey, W. H.; David Britt, R. *Polyhedron* **2013**, *64*, 304.

(54) Robin, M. B.; Day, P. *Adv. Inorg. Chem. Radiochem.* **1968**, *10*, 247.

(55) Hush, N. S. *Chem. Phys.* **1975**, *10*, 361.

(56) Smith, P. F.; Kaplan, C.; Sheats, J. E.; Robinson, D. M.; McCool, N. S.; Mezle, N.; Dismukes, G. C. *Inorg. Chem.* **2014**, *53*, 2113.

(57) Surendranath, Y.; Kanan, M. W.; Nocera, D. G. *J. Am. Chem. Soc.* **2010**, *132*, 16501.

(58) Bediako, D. K.; Costentin, C.; Jones, E. C.; Nocera, D. G.; Savéant, J.-M. *J. Am. Chem. Soc.* **2013**, *135*, 10492.

(59) Ullman, A. M.; Nocera, D. G. *J. Am. Chem. Soc.* **2013**, *135*, 15053.

(60) Costentin, C.; Porter, T. R.; Savéant, J.-M. *J. Am. Chem. Soc.* **2016**, *138*, 5615.

(61) Day, P.; Hush, N. S.; Clark, R. J. H. *Philos. Trans. R. Soc., A* **2008**, *366*, 5.

(62) Glover, S. D.; Lear, B. J.; Salsman, J. C.; Londergan, C. H.; Kubiak, C. P. *Philos. Trans. R. Soc., A* **2008**, *366*, 177.

(63) Glover, S. D.; Goeltz, J. C.; Lear, B. J.; Kubiak, C. P. *Eur. J. Inorg. Chem.* **2009**, *2009*, 585.

(64) Glover, S. D.; Goeltz, J. C.; Lear, B. J.; Kubiak, C. P. *Coord. Chem. Rev.* **2010**, *254*, 331.

(65) Brunschwig, B. S.; Creutz, C.; Sutin, N. *Chem. Soc. Rev.* **2002**, *31*, 168.

(66) Poltavets, V. V.; Croft, M.; Greenblatt, M. *Phys. Rev. B: Condens. Matter Mater. Phys.* **2006**, *74*, 125103.

(67) Westre, T. E.; Kennepohl, P.; DeWitt, J. G.; Hedman, B.; Hodgson, K. O.; Solomon, E. I. *J. Am. Chem. Soc.* **1997**, *119*, 6297.

(68) Iwai, K.; Iwai, M.; Suto, K.; Nakashima, S.; Motoyama, I.; Sano, H.; Ikemoto, I.; Kosugi, N.; Kuroda, H. *Bull. Chem. Soc. Jpn.* **1986**, *59*, 2675.

(69) Glatzel, P.; Mirone, A.; Eeckhout, S. G.; Sikora, M.; Giuli, G. *Phys. Rev. B: Condens. Matter Mater. Phys.* **2008**, *77*, 115133.

(70) Vanko, G.; de Groot, F. M. F.; Huotari, S.; Cava, R. J.; Lorenz, T.; Reuther, M. *ArXiv.org e-Print Arch., Condens. Matter* **2008**, arXiv:082.2744v1 [cond-mat.str-el].

(71) de Groot, F. M. F.; Vankó, G.; Glatzel, P. *J. Phys.: Condens. Matter* **2009**, *21*, 104207.

(72) Risch, M.; Ringleb, F.; Kohlhoff, M.; Bogdanoff, P.; Chernev, P.; Zaharieva, I.; Dau, H. *Energy Environ. Sci.* **2015**, *8*, 661.

(73) Wasinger, E. C.; de Groot, F. M. F.; Hedman, B.; Hodgson, K. O.; Solomon, E. I. *J. Am. Chem. Soc.* **2003**, *125*, 12894.

(74) Hocking, R. K.; DeBeer George, S.; Raymond, K. N.; Hodgson, K. O.; Hedman, B.; Solomon, E. I. *J. Am. Chem. Soc.* **2010**, *132*, 4006.

(75) Cartier dit Moulin, C.; Rudolf, P.; Flank, A. M.; Chen, C. T. *J. Phys. Chem.* **1992**, *96*, 6196.

(76) Glatzel, P.; Bergmann, U. *Coord. Chem. Rev.* **2005**, *249*, 65.

(77) Shvyd'ko, Y. V.; Hill, J. P.; Burns, C. A.; Coburn, D. S.; Brajuskovic, B.; Casa, D.; Goetze, K.; Gog, T.; Khachatryan, R.; Kim, J. H.; Kodituwakku, C. N.; Ramanathan, M.; Roberts, T.; Said, A.; Sinn, H.; Shu, D.; Stoupin, S.; Upton, M.; Wieczorek, M.; Yavas, H. *J. Electron Spectrosc. Relat. Phenom.* **2013**, *188*, 140.

(78) Wang, L.-P.; Van Voorhis, T. *J. Phys. Chem. Lett.* **2011**, *2*, 2200.

(79) Mavros, M. G.; Tsuchimochi, T.; Kowalczyk, T.; McIsaac, A.; Wang, L.-P.; Voorhis, T. V. *Inorg. Chem.* **2014**, *53*, 6386.

(80) Hadt, R. G.; Nemykin, V. N. *Inorg. Chem.* **2009**, *48*, 3982.

(81) Lundberg, M.; Siegbahn, P. E. M. *J. Chem. Phys.* **2005**, *122*, 224103.

(82) Neese, F. *Coord. Chem. Rev.* **2009**, *253*, 526.

(83) Anxolabehere-Mallart, E.; Glaser, T.; Frank, P.; Aliverti, A.; Zanetti, G.; Hedman, B.; Hodgson, K. O.; Solomon, E. I. *J. Am. Chem. Soc.* **2001**, *123*, 5444.

(84) Glaser, T.; Bertini, I.; Moura, J. J. G.; Hedman, B.; Hodgson, K. O.; Solomon, E. I. *J. Am. Chem. Soc.* **2001**, *123*, 4859.

(85) Dey, A.; Jenney, F. E., Jr.; Adams, M. W. W.; Babini, E.; Takahashi, Y.; Fukuyama, K.; Hodgson, K. O.; Hedman, B.; Solomon, E. I. *Science* **2007**, *318*, 1464.

(86) Hadt, R. G.; Sun, N.; Marshall, N. M.; Hodgson, K. O.; Hedman, B.; Lu, Y.; Solomon, E. I. *J. Am. Chem. Soc.* **2012**, *134*, 16701.

(87) Etourneau, J.; Portier, J.; Ménil, F. *J. Alloys Compd.* **1992**, *188*, 1.

(88) Tanabe, Y.; Sugano, S. *J. Phys. Soc. Jpn.* **1954**, *9*, 753.

(89) Buffat, B.; Demazeau, G.; Pouchard, M.; Dance, J. M.; Hagenmuller, P. *J. Solid State Chem.* **1983**, *50*, 33.

(90) Hocking, R. K.; Wasinger, E. C.; de Groot, F. M. F.; Hodgson, K. O.; Hedman, B.; Solomon, E. I. *J. Am. Chem. Soc.* **2006**, *128*, 10442.

(91) Abbate, M.; de Groot, F. M. F.; Fuggle, J. C.; Fujimori, A.; Strebel, O.; Lopez, F.; Domke, M.; Kaindl, G.; Sawatzky, G. A.; Takano, M.; Takeda, Y.; Eisaki, H.; Uchida, S. *Phys. Rev. B: Condens. Matter Mater. Phys.* **1992**, *46*, 4511.

(92) Warda, S. A.; Massa, W.; Reinen, D.; Hu, Z.; Kaindl, G.; de Groot, F. M. F. *J. Solid State Chem.* **1999**, *146*, 79.

(93) de Groot, F. M. F. *Coord. Chem. Rev.* **2005**, *249*, 31.

(94) de Groot, F. M. F.; Hu, Z. W.; Lopez, M. F.; Kaindl, G.; Guillot, F.; Tronc, M. *J. Chem. Phys.* **1994**, *101*, 6570.

(95) Stevens, K. W. H. *Proc. R. Soc. London, Ser. A* **1953**, *219*, 542.

(96) Figgis, B. N. *Trans. Faraday Soc.* **1961**, *57*, 198.

(97) Griffith, J. S. *Proc. R. Soc. London, Ser. A* **1956**, *235*, 23.

(98) Taylor, C. P. S. *Biochim. Biophys. Acta, Protein Struct.* **1977**, *491*, 137.

(99) Cheng, X.; Fabbri, E.; Nachtegaal, M.; Castelli, I. E.; El Kazzi, M.; Haumont, R.; Marzari, N.; Schmidt, T. J. *Chem. Mater.* **2015**, *27*, 7662.

(100) Obashi, M. *Jpn. J. Appl. Phys.* **1977**, *16*, 167.

(101) Juhin, A.; de Groot, F.; Vankó, G.; Calandra, M.; Brouder, C. *Phys. Rev. B: Condens. Matter Mater. Phys.* **2010**, *81*, 115115.

(102) Creutz, C.; Taube, H. *J. Am. Chem. Soc.* **1969**, *91*, 3988.

(103) Tsui, E. Y.; Tran, R.; Yano, J.; Agapie, T. *Nat. Chem.* **2013**, *5*, 293.

(104) Lin, P.-H.; Takase, M. K.; Agapie, T. *Inorg. Chem.* **2015**, *54*, 59.

(105) Krewald, V.; Neese, F.; Pantazis, D. A. *Phys. Chem. Chem. Phys.* **2016**, *18*, 10739.

(106) Evangelisti, F.; Moré, R.; Hodel, F.; Luber, S.; Patzke, G. R. *J. Am. Chem. Soc.* **2015**, *137*, 11076.

(107) Dogutan, D. K.; McGuire, R.; Nocera, D. G. *J. Am. Chem. Soc.* **2011**, *133*, 9178.

(108) Rao, G. R. R.; Hegde, M. S.; Sarma, D. D.; Rao, C. N. R. *J. Phys.: Condens. Matter* **1989**, *1*, 2147.

(109) Uchimoto, Y.; Sawada, H.; Yao, T. *J. Power Sources* **2001**, *97–98*, 326.

(110) Kuiper, P.; Kruizinga, G.; Ghijsen, J.; Sawatzky, G. A.; Verweij, H. *Phys. Rev. Lett.* **1989**, *62*, 221.

(111) Mizokawa, T.; Wakisaka, Y.; Sudayama, T.; Iwai, C.; Miyoshi, K.; Takeuchi, J.; Wadati, H.; Hawthorn, D. G.; Regier, T. Z.; Sawatzky, G. A. *Phys. Rev. Lett.* **2013**, *111*, 056404.

(112) Luo, K.; Roberts, M. R.; Hao, R.; Guerrini, N.; Pickup, D. M.; Liu, Y.-S.; Edström, K.; Guo, J.; Chadwick, A. V.; Duda, L. C.; Bruce, P. G. *Nat. Chem.* **2016**, *8*, 684.